Data supplement for Aggarwal et al., Sex-Specific Distributed White Matter Microarchitectural Alterations in Preadolescent Youths With Anxiety Disorders: A Mega-Analytic Study. Am J Psychiatry (doi: 10.1176/appi.ajp.20221048)

Supplemental Methods

Childhood Opportunity Index: The Childhood Opportunity Index (COI) is a census-derived composite metric of 29 indicators of neighborhood-level resources and conditions spanning three domains: Education, Health and Environment, and Social and Economic (https://www.diversitydatakids.org/child-opportunity-index). It captures facets of children's environment that are relevant to their future health and economic outcomes. COI data were generated by first aggregating home address information for our sample; valid information was available for 230 participants. Individual address information was then used to obtain a geographic identifier (i.e., GeoID) for each of these participants using the following website: https://geocoding.geo.census.gov/geocoder/geographies/addressbatch?form. Finally, GeoIDs were matched to the COI 2.0 Index Data sheet available here: https://data.diversitydatakids.org/dataset/coi20-child-opportunity- index-2-0-database/resource/080cfe52-90aa-4925-beaa-90efb04ab7fb. This data sheet provides subscale and composite COI metric data for GeoIDs, or census tracts, across the country, including metro-, state-, and national-level z-scored. Because our data includes participants from two different states, we used the nationally z-scored composite COI score in our analyses. It is important to note the COI score is not an individual-difference measure; it is a census tract level measure.

DTI acquisition: Images were collected on a 3.0 Tesla GE MR750 scanner (GE Healthcare; Waukesha, WI). In sample 1, UW participants were scanned using an 8-channel head coil. NIH participants from sample 1, all of sample 2, and all of sample 3 were scanned using a 32-channel head coil. Diffusion-weighted MRI scans were obtained using a two-dimensional echo planar imaging diffusion-weighted spin-echo sequence (TR=6500ms, TE=59.6ms, flip angle=90 degrees, matrix=128x128 interpolated to 256x256, FOV=256mm, 2.9mm contiguous slices, echo-planar echo spacing=568μs, b-value of 1000s/mm^2, 48 optimal non-collinear directions and 8 non-diffusion-weighted images). Structural and functional MRI scans were collected during the same scan sessions but are not reported here. Before each scan, children completed mock MRI sessions, which have been shown to reduce movement in pediatric neuroimaging studies (1).

DTI processing, harmonization, and analysis: Methods were comparable to those previously described in Tromp et al., 2019 and Aggarwal et al., 2022 (2,3). Diffusion-weighted volumes from each individual were transformed into a 3-dimensional diffusion tensor for each voxel in the brain using the following procedures. FSL (4) tools for rigid registration were used to correct distortions resulting from head motion and eddy currents (5). The corresponding gradient direction matrix was corrected for the applied rotations after rigid registration. The brain was skull stripped using the FSL's brain extraction tool (4). Robust estimation of tensors by outlier rejection (RESTORE, as implemented in Camino software) (6) was used to minimize influence

of noise on tensor calculation, a step particularly important in image samples of young/clinical populations that are more sensitive to reduced image quality. RESTORE uses an average noise estimation to determine which diffusion measurements are outliers and excludes those from tensor computation; it has been shown to increase the reliability of tensor estimation in clinical populations (7). Resulting DTI scans contained 3 major vectors for each voxel in the brain that together model water diffusion as shaped by local tissue microstructure.

In order to compare diffusion measures across participants, scans were normalized across all participants to create a study-specific template that was then warped to MNI-152 standard space via rigid, affine, and diffeomorphic (i.e., nonlinear) registrations. Individual tensor maps were generated in MNI space. These steps were performed using a high-dimensional registration method that incorporates tensor orientation (DTI-TK) (8), a technique that outperforms intensity-based normalization of diffusion images and results in improved white matter shape and architecture representation (9,10). The population template was constructed via multiple registration iterations and then aligned to the 1mm isotropic MNI-152 template; this warp was then applied to all images. In MNI152 space, scalar maps for fractional anisotropy (FA), mean diffusivity (MD), radial diffusivity (RD), and axial diffusivity (XD) were calculated for each image. Finally, images were smoothed with a 4-mm full width at half maximum (FWHM) kernel. We note that field maps were not available for the full sample, so field map-based EPI distortion correction was not performed in our analyses. However, some studies have indicated that, in the absence of available field maps, non-linear registration of diffusion images to a structural image can be used as a substitute to help account for EPI-induced distortions (11), as detailed above as part of image normalization/registration process.

The population template in standard MNI space was used for deterministic tractography to delineate tracts of interest. Whole-brain fiber tracking was performed using Camino software, which implements a fourth-order Runge-Kutta method combined with a tensor deflection (TEND) algorithm for optimal estimation of the fiber tracking directions (12,13). Fiber tracking was terminated in voxels where FA was below 0.1 or where the angle between consecutive streamline steps was greater than 90 degrees. Seven fiber pathways were iteratively delineated in template space using anatomically defined waypoints (14–17) in TrackVis, a 3D tract visualization program (18). The 7 WM tracts of interest were selected based on substantial literature implicating alterations in these tracts in anxiety disorders and other internalizing disorders, in both adult and pediatric samples. In addition to the literature highlighted in relation to the UF, there is work suggesting other cortico-limbic association pathways may be affected in those with pathological anxiety and/or emotional dysregulation, including the cingulum bundle (CING) (19,20), the superior longitudinal fasciculus (SLF) (21,22), the fornix (FX) (23), and the inferior fronto-occipital fasciculus (IFO) (22,24). Additionally, several publications have reported alterations in the projection fibers of the internal capsule (IC) (22,25) and commissural fibers of the corpus callosum (CC) (19,26) in patients with anxious and internalizing pathology. In turn, these 7 tracts were included in our analysis.

In order to quantify the microstructure of entire white matter structures, weighted means were calculated per tract, per participant. The weighted mean of a tract was calculated by first creating a scalar image of the number of fibers in the tract passing through each voxel as a proportion of the total number of fibers in that tract. This weighting factor was then multiplied by the value of the diffusion measure in that voxel and averaged across the whole tract to produce the mean weighted scalar value for each tract (27). This approach enables differential weighting of voxels that have higher fiber counts, observed frequently in areas more central to the white matter tract of interest. Given no a priori hypotheses regarding laterality, right and left

hemisphere metrics were averaged to generate bilateral tract values. Importantly, tract-based analyses allow for detection of pervasive but subtle differences that are distributed across the length of a tract which may be missed using conventional voxel-based methods. In turn, this method is well-suited to identify tract-based associations in which alterations at any point in a tract might alter the efficiency of communication across a WM pathway.

To optimize the comparison of multi-site and multi-sample data and account for coil differences and disparate time intervals in data collection, we performed data harmonization on both the tract- and voxel-level data. The neuroCombat (28,29) and neuroHarmonize (30,31) programs were used to perform harmonization on the tract- based and voxel-based data, respectively. For both tract- and voxel-level harmonization, the dataset was separated in five data "batches" based on Site (UW vs. NIH), Sample (1 vs. 2. Vs. 3), and Coil (8- vs. 32- channel head coil). This resulted in five possible "batch" designations: Batch A (UW, Sample 1, 32-channel head coil); Batch B (NIH, Sample 1, 32-channel head coil); Batch C (UW, Sample 2, 32-channel head coil); Batch D (UW, Sample 3, 8-channel head coil); and Batch E (NIH, Sample 3, 32-channel head coil). For tract- level data harmonization, the neuroCombat algorithm was provided DTI metric data for each of the seven tracts of interest and the batch designation for each subject's data, as well as the model terms so as to allow the algorithm to preserve the variance of interest. Tract-level data harmonization was performed separately for FA, MD, RD, and XD. For voxel-level data harmonization, the neuroHarmonize algorithm was provided voxelwise diffusion parameter maps and the batch designation for each subject's data, in addition to the model predictors. Voxelwise data harmonization was also performed separately for FA, MD, RD, and XD. For both tract- and voxel-level data harmonization, batch information was provided, and the following analytic model was specified: *DTI metric ~ Group*Sex + Group + Sex + Age*. In all subsequent analyses at the tract- and voxel-level using the harmonized data, the above model was implemented, given that harmonization accounted for the effects of Site, Sample, and Coil.

Statistical analysis for voxelwise DTI analyses: Because FA changes in grey matter (GM) are difficult to interpret, voxelwise analyses were restricted to a liberal WM mask. The WM mask was generated by applying the FAST (FMRIB's Automated Segmentation Tool) algorithm, an MR image segmentation tool in FSL, to the MNI T1 template image to produce WM, GM, and cerebrospinal fluid (CSF) segmentations. The resulting WM segmentation was binarized and used as the WM mask for *randomise* analyses (see Figure S1).

Steroid hormone collection and analyses: Saliva samples were collected on the day of MRI scanning. Testosterone and estradiol levels were measured in separate enzyme immunoassays using kits purchased from Salimetrics (State College, PA). Prior to each assay, saliva was thawed and spun at 1,500 x g for 15 min at room temperature to remove particulate. The supernatant was assayed in duplicate following manufacturer's instructions. Samples that had assay results with CV% > 20 were repeated. The inter-assay CVs were determined using the high and low controls provided by the kits. For testosterone, the high control had a concentration of 186.9 ± 2.8 pg/ml and a CV of 4.2%, and the low control had a concentration of 28.8 ± 0.9 pg/ml and a CV of 8.5%. For estradiol, the high control had a concentration of 22.5 ± 0.4 pg/ml and a CV of 5.4%, and the low control had a concentration of 6.8 ± 0.1 pg/ml and a CV of 3.2%. For the subset of participants with usable sex hormone level data, testosterone and estradiol levels were first square-root transformed, and then linear regression models assessed three-way interactions between group (anxiety disorder vs. healthy volunteer), sex (male vs. female), and sex hormone (testosterone or estradiol) to investigate potential moderating effects of sex hormones on sex-specific anxiety-WM associations.

Supplemental Results

Voxelwise analyses of MD, RD, and XD: RD was increased in children with anxiety disorders relative to healthy volunteers, indicated by a main effect of group in clusters that overlapped with portions of the UF, EC, SS, IFOF, IFL, IC, STRIA, FX, CR, CBP, CP, CC, CST, CING, and SLF (TFCE P<0.05, FWE-corrected) (see Table S3 and Figure S3A). No significant group-by-sex interactions were found for RD. Separate RD analyses of the males and the females revealed no anxiety disorder-related effects in females, whereas males had significant RD reductions in regions consistent with those detected in the main effect of group, in addition to several other WM clusters throughout the brain (TFCE P<0.05, FWE-corrected) (see Table S3 and Figure S3C). Analyses of MD and XD did not reveal any significant effects of group or group-by-sex interactions.

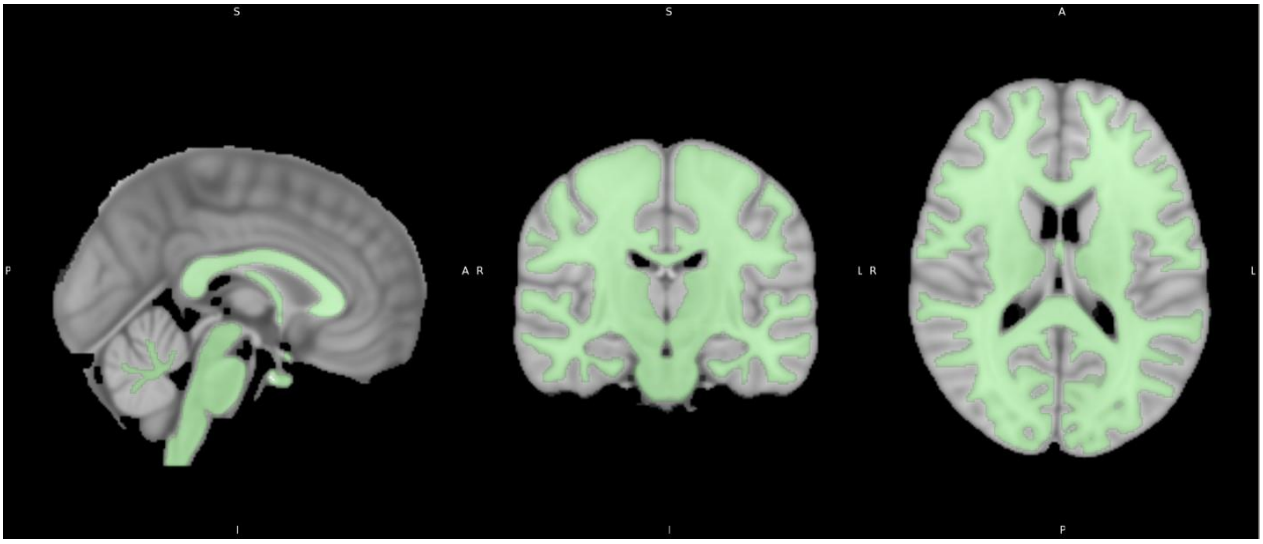

FIGURE S1. Binary WM mask (in green) in MNI space used for voxelwise analyses of DTI metrics (FA, MD, RD, XD).

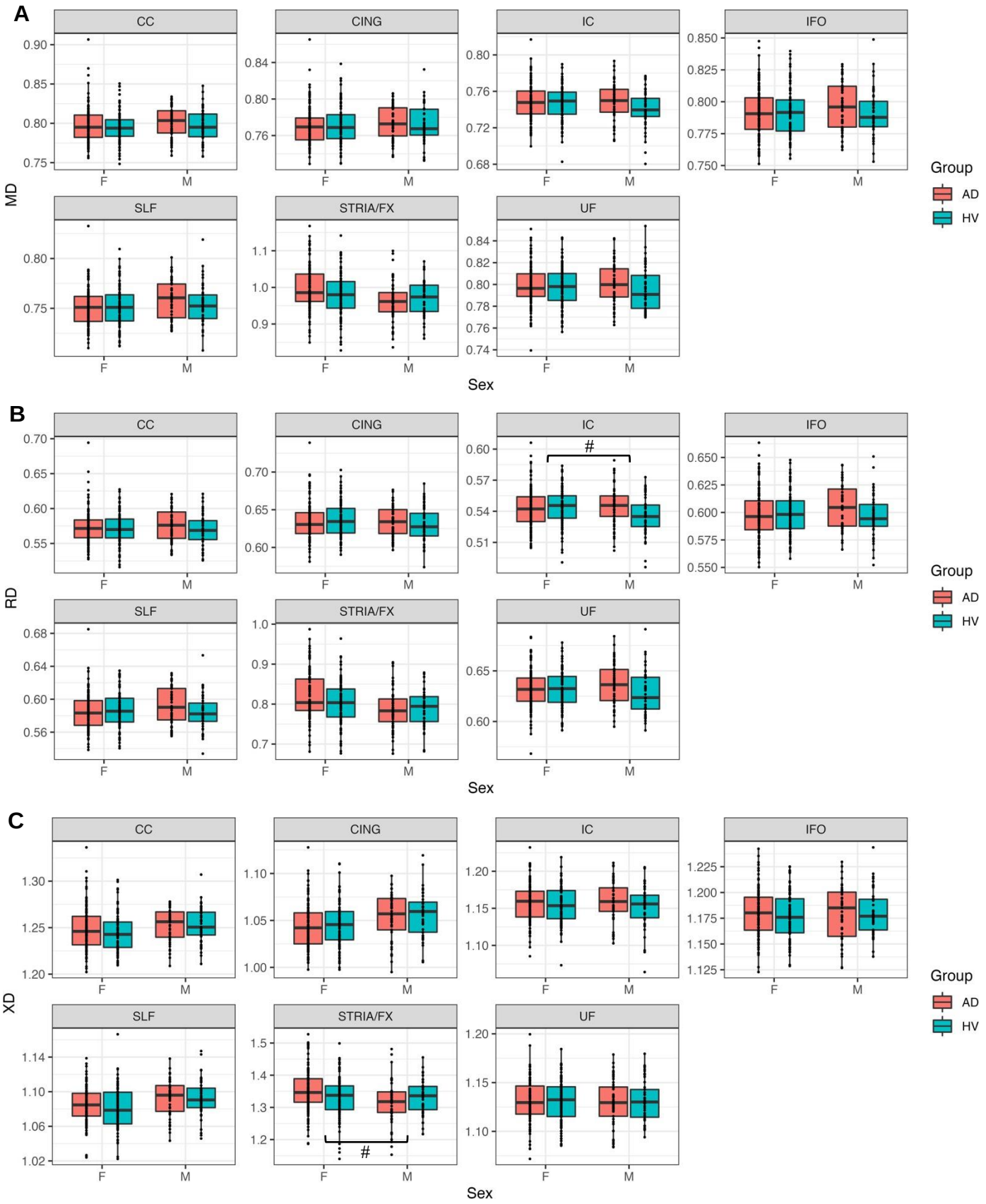

FIGURE S2. Group-by-sex interactions in relation to MD, RD, and XD in seven bilateral WM tracts. Panels A, B, and C represent the group-by-sex interaction in relation to MD, RD, and XD, respectively in the 7 WM tracts of interest. Red denotes children with anxiety disorders (n=163); blue denotes healthy volunteers (n=132). Plots connoted with a pound sign (#) indicate a group-by-sex interaction significant at the uncorrected threshold (p<0.05, uncorrected).

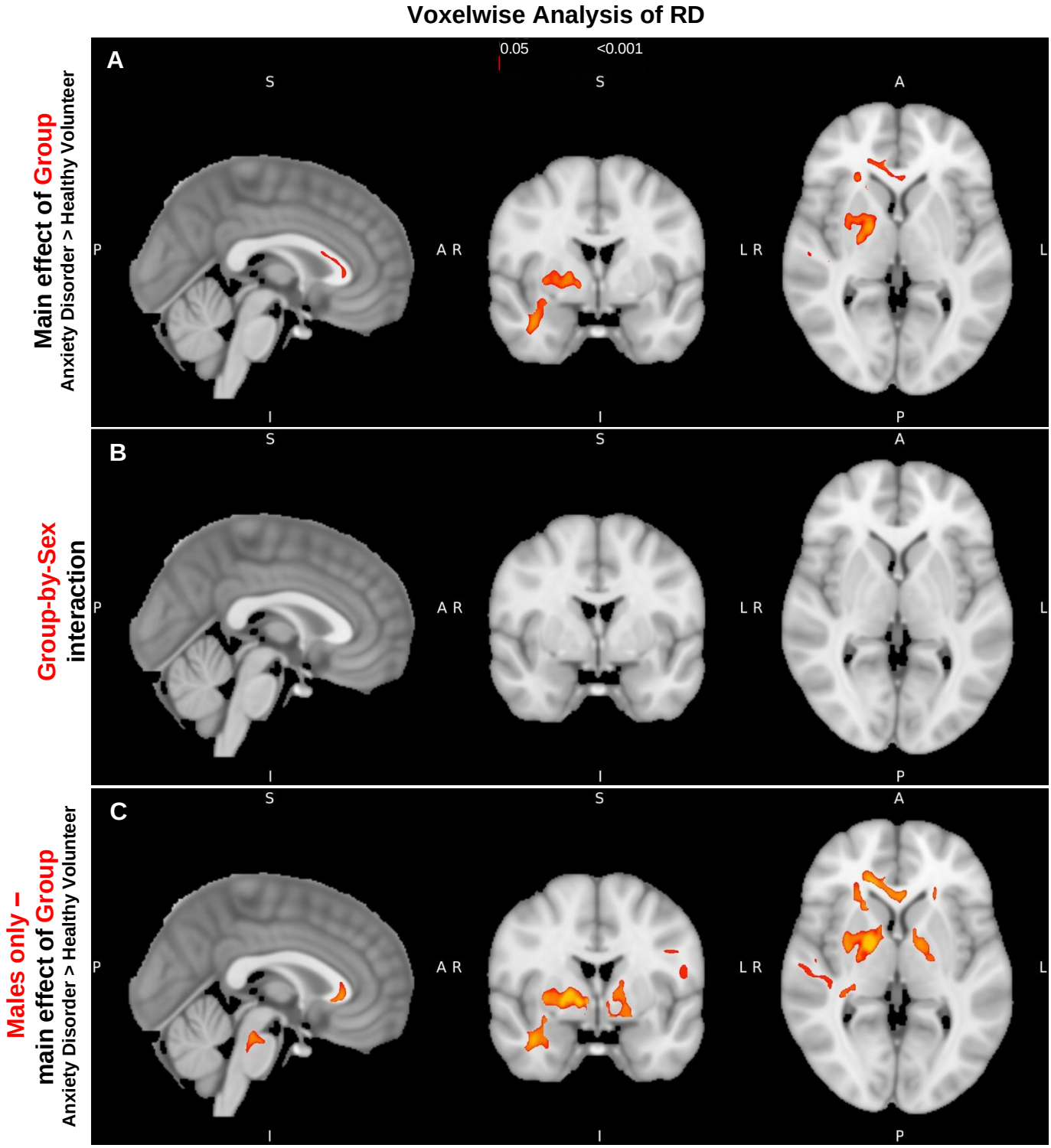

FIGURE S3. Voxelwise analysis of group differences and group-by-sex interactions across whole-brain WM RD. All analyses reflect harmonized data and include age as a covariate. All three panels show sagittal, coronal, and transverse views at MNI coordinates [92, 126, 74]. Results shown are using threshold-free cluster enhancement (TFCE) and corrected for multiple comparisons using the family-wise error rate ($p<0.05$, FWE-corrected). A) Voxels in which RD is significantly greater in children with anxiety disorders compared to healthy volunteers across the combined sample. B) Voxels in which there is a significant group-by-sex interaction in relation to RD. C) In the males alone, voxels in which RD is significantly greater in boys with anxiety disorders compared to healthy volunteer boys. In analyses of females alone, there were no significant differences in RD between girls with anxiety disorders and healthy volunteer girls.

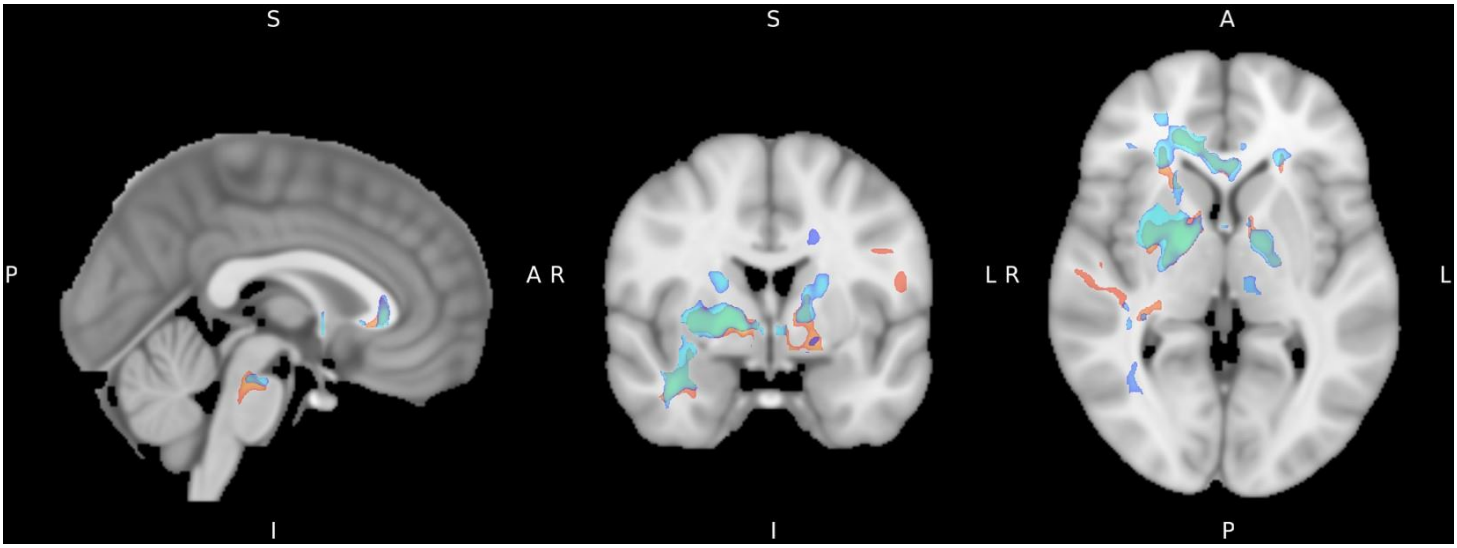

FIGURE S4. Overlap of voxel maps depicting the main effects of group FA and RD in males alone (i.e., overlap of Figure 2C and Figure S3C). Results shown are TFCE P<0.05; FWE-corrected. Blue voxels indicate regions in which FA is significantly decreased in boys with anxiety disorders relative to healthy volunteer boys, while red voxels indicate regions in which RD is significantly increased in boys with anxiety disorders relative to healthy volunteer boys. Note the prominent overlap in the pattern of reduced FA and greater RD in boys with anxiety disorders.

	FA – Main Effects of Age and Sex					
	Age			Sex		
Bilateral WM Tract	t	df	p-value	t	df	p-value
CC	5.373	290	<0.001	-1.506	290	0.133
CING	8.280	290	<0.001	-4.442	290	<0.001
IC	7.493	290	<0.001	0.313	290	0.755
IFO	6.626	290	<0.001	0.274	290	0.784
SLF	5.139	290	<0.001	-0.602	290	0.548
STRIA/FX	1.095	290	0.274	-2.561	290	0.011
UF	4.978	290	<0.001	0.057	290	0.954

	FA – Three-Way Interactions with Group*Sex											
	Age*Sex*Group			Tanner*Sex*Group			Testosterone*Sex*Group			Estradiol*Sex*Group		
Bilateral WM Tract	t	df	p-value	t	df	p-value	t	df	p-value	t	df	p-value
CC	-0.278	287	0.781	-1.167	265	0.244	-0.051	203	0.960	1.146	202	0.253
CING	1.098	287	0.273	0.066	265	0.947	-0.075	203	0.941	1.031	202	0.304
IC	0.902	287	0.368	0.562	265	0.574	1.321	203	0.188	0.471	202	0.638
IFO	0.890	287	0.374	0.000	265	1.000	0.688	203	0.492	0.641	202	0.523
SLF	-0.658	287	0.511	-0.534	265	0.594	-0.037	203	0.971	0.244	202	0.808
STRIA/FX	0.143	287	0.886	-1.259	265	0.209	0.682	203	0.496	1.431	202	0.154
UF	-0.107	287	0.915	-0.121	265	0.904	0.140	203	0.889	0.690	202	0.491

	FA – Analyses Related to the Childhood Opportunity Index (COI)								
	Analysis in COI Subset (w/o cont. for COI)			Analysis cont. for COI					
	Group*Sex			Group*Sex			COI		
Bilateral WM Tract	t	df	p-value	t	df	p-value	t	df	p-value
CC	1.769	225	0.078	1.777	224	0.077	0.286	224	0.775
CING	1.716	225	0.088	1.698	224	0.091	-0.241	224	0.810
IC	2.031	225	0.044	2.036	224	0.043	0.249	224	0.803
IFO	2.400	225	0.017	2.371	224	0.019	-0.423	224	0.673
SLF	0.906	225	0.366	0.925	224	0.356	0.445	224	0.657
STRIA/FX	1.839	225	0.067	1.881	224	0.061	0.890	224	0.374
UF	2.344	225	0.020	2.296	224	0.023	-0.877	224	0.382

	FA – Analyses Controlling for Age*Sex, Age*Tanner, CDI, and CPRS								
	Cont. for Age*Sex + Age*Tanner			Cont. for CDI			Cont. for CPRS		
	Group*Sex			Group*Sex			Group*Sex		
Bilateral WM Tract	t	df	p-value	t	df	p-value	t	df	p-value
CC	2.669	265	0.008	2.875	187	0.005	2.619	276	0.009
CING	1.318	265	0.189	1.946	187	0.053	1.875	276	0.062
IC	2.006	265	0.046	1.268	187	0.207	2.367	276	0.019
IFO	2.479	265	0.014	2.893	187	0.004	2.844	276	0.005
SLF	2.272	265	0.024	2.102	187	0.037	2.656	276	0.008
STRIA/FX	1.735	265	0.084	3.051	187	0.003	1.922	276	0.056
UF	3.553	265	<0.001	3.953	187	<0.001	2.982	276	0.003

	FA – Interactions Between SCARED Measures and Sex					
	Child-SCARED*Sex			Parent-SCARED*Sex		
Bilateral WM Tract	t	df	p-value	t	df	p-value
CC	0.455	281	0.650	1.542	281	0.1242
CING	1.798	281	0.073	0.753	281	0.452
IC	1.017	281	0.310	1.426	281	0.155
IFO	0.578	281	0.564	1.442	281	0.151
SLF	0.917	281	0.360	1.398	281	0.163
STRIA/FX	0.090	281	0.928	1.301	281	0.194
UF	0.296	281	0.767	1.428	281	0.154

TABLE S1. Main effects of age and sex; three-way interactions between developmental covariates and the Group-by-Sex term; COI covariate analyses; Age*Sex, Age*Tanner, CDI, and CPRS covariate analyses; and SCARED-by-Sex effects in relation to FA in the 7 WM tracts analyzed via tractography. Tanner stages were log- transformed; testosterone, square-root transformed; estradiol, square-root transformed. All analyses controlled for age.

	MD							
	Combined Sample				Boys		Girls	
	Group		**Group-by-Sex**		**Group**		**Group**	
Bilateral WM Tract	**t**	**p-value**	**t**	**p-value**	**t**	**p-value**	**t**	**p-value**
CC	1.470	0.143	-0.416	0.678	1.195	0.235	0.917	0.361
CING	0.164	0.870	-0.767	0.444	0.557	0.579	-0.506	0.613
IC	1.868	0.063	-1.640	0.102	2.041	0.044	0.206	0.837
IFO	1.281	0.201	-1.155	0.249	1.445	0.152	0.122	0.903
SLF	1.246	0.214	-1.172	0.242	1.405	0.163	0.083	0.934
STRIA/FX	0.812	0.417	1.935	0.054	-0.736	0.464	2.343	0.020
UF	1.389	0.166	-1.082	0.280	1.417	0.160	0.279	0.780
	RD							
	Combined Sample				Boys		Girls	
	Group		**Group-by-Sex**		**Group**		**Group**	
Bilateral WM Tract	**t**	**p-value**	**t**	**p-value**	**t**	**p-value**	**t**	**p-value**
CC	1.636	0.103	-1.051	0.294	1.688	0.095	0.517	0.606
CING	0.570	0.569	-1.171	0.243	1.110	0.270	-0.500	0.618
IC	1.964	0.050	-2.263	0.024	2.518	0.014	-0.258	0.797
IFO	1.473	0.142	-1.960	0.051	2.089	0.039	-0.408	0.683
SLF	1.220	0.224	-1.885	0.060	1.865	0.065	-0.570	0.57
STRIA/FX	1.016	0.310	1.555	0.121	-0.363	0.718	2.173	0.031
UF	2.067	0.040	-1.850	0.065	2.242	0.027	0.197	0.844
	XD							
	Combined Sample				Boys		Girls	
	Group		**Group-by-Sex**		**Group**		**Group**	
Bilateral WM Tract	**t**	**p-value**	**t**	**p-value**	**t**	**p-value**	**t**	**p-value**
CC	0.820	0.413	0.933	0.352	-0.096	0.924	1.485	0.139
CING	-0.708	0.479	0.124	0.902	-0.536	0.594	-0.498	0.619
IC	1.393	0.165	-0.521	0.603	1.105	0.272	0.784	0.434
IFO	0.572	0.568	0.564	0.573	0.017	0.987	1.004	0.316
SLF	0.885	0.377	0.645	0.519	0.129	0.898	1.342	0.181
STRIA/FX	0.379	0.705	2.448	0.015	-1.300	0.197	2.449	0.015
UF	-0.164	0.870	0.477	0.634	-0.384	0.702	0.286	0.775

TABLE S2. Tract-level analysis of group differences and group-by-sex interactions in the MD, RD, and XD of seven bilateral WM tracts. All analyses reflect harmonized data and include age as a covariate.

FA - Group

Clust #	Vol. (mm^3)	Location	Hemi	Peak MNI Coordinates X	Y	Z
1	9193	CC; CR; EC; UF	R/L	105	161	71
2	3560	IC; CR; EC	R/L	110	122	73
3	1250	IC; CR	L	74	122	74
4	1056	CC; CR	L	72	156	71
5	126	SS; ILF; IFOF	R	143	97	61
6	85	EC	R	125	137	66
7	80	CP	R	79	106	59
8	71	SS; ILF; IFOF	R	133	115	60
9	29	IC	L	82	104	73

RD - Group

Clust #	Vol. (mm^3)	Location	Hemi	Peak MNI Coordinates X	Y	Z
1	4550	EC; IC; UF; SS; ILF; IFOF	R	109	122	73
2	1419	CC; CR	R/L	104	162	67
3	1216	CR; IC	R	121	156	61
4	305	SS; ILF; IFOF; IC	R	129	105	60
5	137	CP; CST	R/L	95	101	48
6	75	ATR	R	146	106	74
7	59	CP	R	107	107	61
8	21	ILF; IFOF	R	143	97	61
9	15	CP	R	99	114	58
10	7	ILF/IFOF	R	141	102	57
11	4	IC	L	87	129	68

FA – Group-by-Sex

Clust #	Vol. (mm^3)	Location	Hemi	Peak MNI Coordinates X	Y	Z
1	9225	EC; CR; IC; SFOF; CC; CING; UF	R/L	121	156	62
2	4418	AC; ATR; EC; IC; CR; CP	R	121	130	71
3	2016	CP; IC	L	78	105	60
4	1482	CP; CST; CBP; ML	R/L	95	97	47
5	1273	IC; CR; EC	L	69	134	84
6	793	CR; EC; IC; SFOF	R	117	118	86
7	639	CR	R	111	98	114
8	499	CBP	R	113	87	31
9	450	CST	R	100	94	136
10	411	CST	L	81	107	131
11	408	CR; EC	L	66	155	71
12	407	CP	R	107	107	61
13	362	CC; CR	L	72	102	103
14	295	IC; CR	L	67	148	85
15	254	CBP	L	71	85	31
16	216	SLF	R	140	129	83
17	191	SLF	L	86	96	122
18	181	CC; CR	L	74	122	107
19	180	CST	L	83	96	141
20	162	SLF	R	133	80	91
21	91	CST	L	68	103	127
22	70	CST	L	57	107	128
23	56	SS; ILF; IFOF; UF	L	49	110	55
24	49	SLF	R	119	93	123
25	36	SLF	R	130	96	101
26	28	CST	L	74	100	132
27	22	ILF; UF	R	133	119	43
28	18	CST	L	78	86	136
29	5	CP	R	96	119	59

FA – Group - MALES

Clust #	Vol. (mm^3)	Location	Hemi	Peak MNI Coordinates X	Y	Z
1	46967	ILF; SLF; MLF; IFOF; UF; AF; CST; CING; CR; IC; EC; SFOF; CC; CP; FX	R/L	133	120	40
2	1326	SLF; CST	L	80	106	133
3	498	CST	R	102	98	138
4	335	AF; SLF; EC	R	133	80	90
5	301	CING; CC; CR	L	74	124	106
6	231	UF; FX; ILF; IFOF; SS	L	50	114	51
7	213	CBP	R	107	65	40
8	209	CBP	R	95	70	44
9	130	CC	L	82	122	99
10	120	CING; FX	L	64	119	41
11	89	CST; SLF	L	71	88	127
12	89	IFOF; UF	R	113	172	61
13	82	CST	L	84	83	143
14	65	AC	L	78	126	60
15	57	ILF	R	138	65	60
16	34	CC	R	94	115	95
17	31	IFOF	L	50	100	59
18	16	ILF	L	43	93	60
19	11	SLF	L	47	117	90
20	4	IFOF	L	49	93	62

RD – Group - MALES

Clust #	Vol. (mm^3)	Location	Hemi	Peak MNI Coordinates X	Y	Z
1	31042	IFOF; ATR; CBP; CST; UF; AC; CING; CC; CR; CP; SS; ILF; IC; SLF	R/L	108	153	60
2	1758	AF; SLF	L	48	118	90
3	1281	ILF; MLF; IFOF; SS	L	44	92	58
4	110	SLF	L	54	101	107
5	44	SLF; AF	L	59	133	91

TABLE S3. Main effect of group in the full sample on FA, RD, and MD (yellow headings); group-by-sex interactions in relation to FA and RD (green headings); and main effect of group in the males alone on FA and RD (blue headings) in voxelwise analyses (TFCE P<0.05, FWE-corrected). Description of clusters in which FA, RD, or MD is significantly reduced (FA) or increased (MD, RD) in children with anxiety disorders compared to healthy volunteers (in the full sample and in males alone), as well group-by-sex interactions in relation to FA and RD. Tract abbreviations: AF=arcuate fasciculus; AC=anterior commissure; ATR=anterior thalamic radiation; CBP=cerebellar peduncle; CP=cerebral peduncle; CING=cingulum; CR=corona radiata; CC=corpus callosum; CST=corticospinal tract; EC=external capsule; FX=fornix; IFOF=inferior fronto-occipital fasciculus; ILF=inferior longitudinal fasciculus; IC=internal capsule; ML=medial lemniscus; MLF=middle longitudinal fasciculus; PTR=posterior thalamic radiation; SS=sagittal striatum; STRIA=stria terminalis; SFOF=superior fronto-occipital fasciculus; SLF=superior longitudinal fasciculus; STR=superior thalamic radiation; UF=uncinate fasciculus.

REFERENCES

1. Bie HMA de, Boersma M, Wattjes MP, Adriaanse S, Vermeulen RJ, Oostrom KJ, et al. Preparing children with a mock scanner training protocol results in high quality structural and functional MRI scans. Eur J Pediatr. 2010;169(9):1079–85.

2. Tromp DPM, Williams LE, Fox AS, Oler JA, Roseboom PH, Rogers GM, et al. Altered Uncinate Fasciculus Microstructure in Childhood Anxiety Disorders in Boys But Not Girls. American Journal of Psychiatry. 2019 Mar;176(3):208–16.

3. Aggarwal N, Williams LE, Tromp DPM, Pine DS, Kalin NH. A dynamic relation between whole-brain white matter microstructural integrity and anxiety symptoms in preadolescent females with pathological anxiety. Transl Psychiat. 2022;12(1):57.

4. Jenkinson M, Beckmann CF, Behrens TEJ, Woolrich MW, Smith SM. FSL. Neuroimage. 2012;62(2):782–90.

5. Leemans A, Jones DK. The B-matrix must be rotated when correcting for subject motion in DTI data. Magnet Reson Med. 2009;61(6):1336–49.

6. Camino: Open-Source Diffusion-MRI Reconstruction and Processing - 02759.pdf [Internet]. [cited 2021 Jun 24]. Available from: https://afni.nimh.nih.gov/sscc/staff/rwcox/ISMRM_2006/ISMRM%202006%20-%203340/files/02759.pdf

7. Chang LC, Jones DK, Pierpaoli C. RESTORE: Robust estimation of tensors by outlier rejection. Magnet Reson Med. 2005;53(5):1088–95.

8. Zhang H, Yushkevich P, Alexander D, Gee J. Deformable registration of diffusion tensor MR images with explicit orientation optimization. Med Image Anal. 2006;10(5):764–85.

9. Zhang H, Avants BB, Yushkevich PA, Woo JH, Wang S, McCluskey LF, et al. High-Dimensional Spatial Normalization of Diffusion Tensor Images Improves the Detection of White Matter Differences: An Example Study Using Amyotrophic Lateral Sclerosis. Ieee T Med Imaging. 2007;26(11):1585–97.

10. Adluru N, Zhang H, Fox AS, Shelton SE, Ennis CM, Bartosic AM, et al. A diffusion tensor brain template for rhesus macaques. Neuroimage. 2011;59(1):306–18.

11. Wang S, Peterson DJ, Gatenby JC, Li W, Grabowski TJ, Madhyastha TM. Evaluation of Field Map and Nonlinear Registration Methods for Correction of Susceptibility Artifacts in Diffusion MRI. Front Neuroinformatics. 2017;11:17.

12. Basser PJ, Pajevic S, Pierpaoli C, Duda J, Aldroubi A. In vivo fiber tractography using DT-MRI data. Magnet Reson Med. 2000;44(4):625–32.

13. Lazar M, Weinstein DM, Tsuruda JS, Hasan KM, Arfanakis K, Meyerand ME, et al. White matter tractography using diffusion tensor deflection. Hum Brain Mapp. 2003;18(4):306–21.

14. Catani M, Howard RJ, Pajevic S, Jones DK. Virtual in vivo interactive dissection of white matter fasciculi in the human brain. Neuroimage. 2002;17(1):77–94.

15. Catani M, Thiebautdeschotten M. A diffusion tensor imaging tractography atlas for virtual in vivo dissections. Cortex. 2008;44(8):1105–32.

16. Mori S, Kaufmann WE, Davatzikos C, Stieltjes B, Amodei L, Fredericksen K, et al. Imaging cortical association tracts in the human brain using diffusion-tensor-based axonal tracking. Magnet Reson Med. 2002;47(2):215–23.

17. Wakana S, Jiang H, Nagae-Poetscher LM, Zijl PCM van, Mori S. Fiber tract-based atlas of human white matter anatomy. Radiology. 2003;230(1):77–87.

18. TrackVis [Internet]. [cited 2021 Jul 15]. Available from: http://trackvis.org/

19. Hung Y, Uchida M, Gaillard SL, Woodworth H, Kelberman C, Capella J, et al. Cingulum-Callosal White- Matter Microstructure Associated with Emotional Dysregulation in Children: A Diffusion Tensor Imaging Study. Neuroimage Clin. 2020;27:102266.

20. Zhang Y, Li L, Yu R, Liu J, Tang J, Tan L, et al. White matter integrity alterations in first episode, treatment- naive generalized anxiety disorder. J Affect Disorders. 2013;148(2–3):196–201.

21. Baur V, Hänggi J, Rufer M, Delsignore A, Jäncke L, Herwig U, et al. White matter alterations in social anxiety disorder. J Psychiatr Res. 2011;45(10):1366–72.

22. Liao M, Yang F, Zhang Y, He Z, Su L, Li L. White matter abnormalities in adolescents with generalized anxiety disorder: a diffusion tensor imaging study. Bmc Psychiatry. 2014;14(1):41.

23. Modi S, Trivedi R, Singh K, Kumar P, Rathore RKS, Tripathi RP, et al. Individual differences in trait anxiety are associated with white matter tract integrity in fornix and uncinate fasciculus: Preliminary evidence from a DTI based tractography study. Behav Brain Res. 2013;238:188–92.

24. Lai CH, Wu YT. Fronto-occipital fasciculus, corpus callosum and superior longitudinal fasciculus tract alterations of first-episode, medication-naïve and late-onset panic disorder patients. J Affect Disorders. 2013;146(3):378–82.

25. Hyett MP, Perry A, Breakspear M, Wen W, Parker GB. White matter alterations in the internal capsule and psychomotor impairment in melancholic depression. Plos One. 2018;13(4):e0195672.

26. Westlye LT, Bjørnebekk A, Grydeland H, Fjell AM, Walhovd KB. Linking an Anxiety-Related Personality Trait to Brain White Matter Microstructure: Diffusion Tensor Imaging and Harm Avoidance. Arch Gen Psychiat. 2011;68(4):369–77.

27. Tromp D. Calculate tract based weighted means [Internet]. [cited 2021 Jul 15]. Available from: https://www.authorea.com/users/226778/articles/284738-calculate-tract-based-weighted- means?commit=466a6f14b3577bd8592ab0b000b8073fd71a88e9

28. GitHub - Jfortin1/neuroCombat_Rpackage: neuroCombat R package [Internet]. [cited 2023 Jul 9]. Available from: https://github.com/Jfortin1/neuroCombat_Rpackage

29. Fortin JP, Parker D, Tunç B, Watanabe T, Elliott MA, Ruparel K, et al. Harmonization of multi-site diffusion tensor imaging data. Neuroimage. 2017;161:149–70.

30. GitHub - rpomponio/neuroHarmonize: Harmonization tools for multi-site neuroimaging analysis. Implemented as a python package. Harmonization of MRI, sMRI, dMRI, fMRI variables with support for NIFTI images. Complements the work in Neuroimage by Pomponio et al. (2019). [Internet]. [cited 2023 Jul 9]. Available from: https://github.com/rpomponio/neuroHarmonize

31. Pomponio R, Erus G, Habes M, Doshi J, Srinivasan D, Mamourian E, et al. Harmonization of large MRI datasets for the analysis of brain imaging patterns throughout the lifespan. NeuroImage. 2020;208:116450.